Preparation of novel high permeability and antifouling polysulfone-vanillin membrane

Sudesh Yadav[1], Ibrar Ibrar[1], Ali Altaee[1,*], Sébastien Déon[2], John Zhou[1]

1: Centre for Green Technology, School of Civil and Environmental Engineering, University of Technology Sydney, 15 Broadway, NSW, 2007, Australia

2: Institut UTINAM (UMR CNRS 6213), Université de Bourgogne-Franche-Comté, 16 Route de Gray, 25030 Besançon Cedex, France

* Corresponding author email address: ali.altaee@uts.edu.au

Graphical Abstract

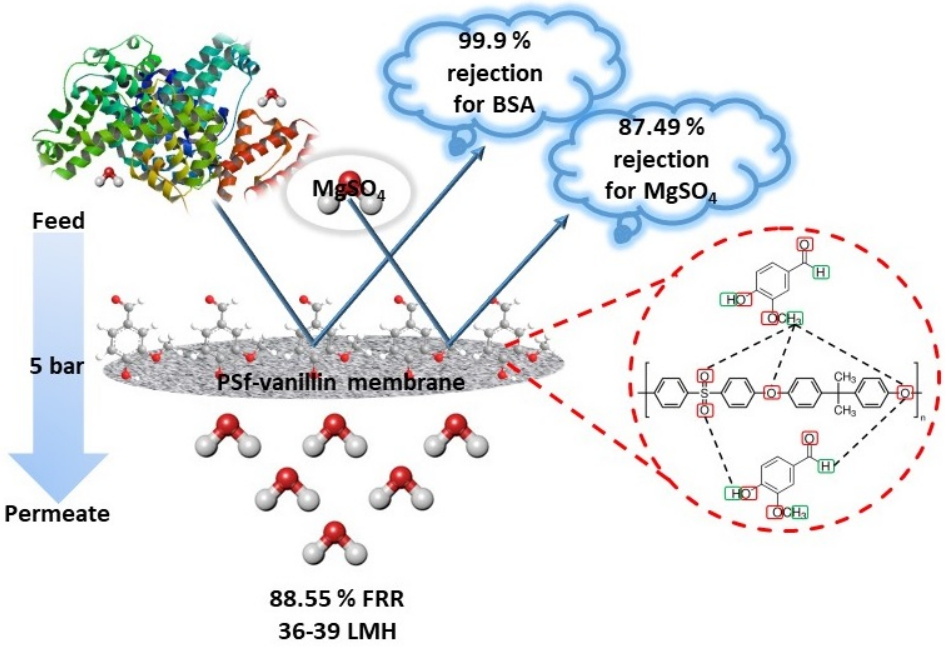

Abstract

A novel high-performance nanofiltration membrane was fabricated by a simple and scalable route involving in situ cross-linking of hydrophilic, cheap, and environmentally friendly vanillin as antifouling agent with polysulfone (PSf) for salt rejection performance. Vanillin acts as a porogen, which induces a negative surface charge on the membrane surface due to the presence of polar functional groups like alcohol and aldehyde. The surface properties, including charge, morphology, and hydrophilicity, were investigated in detail using analytical instruments. The nanofiltration performance of the fabricated PSf-vanillin membranes was dependent on the percentage of vanillin added in the casting solution. The PSf-vanillin membrane antifouling tests were evaluated using 200 mg/L bovine serum albumin (BSA), and results showed 99% rejection with 88.55% flux recovery ratio. Performance studies were compared with commercially available TRISEP® UA60 nanofiltration membrane. PSf-vanillin membrane M_2 showed higher $MgSO_4$ (87.49%), NaCl (25.78%) rejection with excellent antifouling properties compared to commercial UA60 membrane. It is believed that charged membranes are the building blocks for the development of future generation desalination membranes possessing high permeability and selectivity index. The developed membranes have potential niche application in the pre-treatment of feed solution.

Keywords*:* PSf-vanillin membrane; nanofiltration membrane; antifouling membrane; desalination; purification.

Introduction

Water consumption has increased drastically due to the increase in industrial activities and population growth [1, 2]. As a result, freshwater resources are depleting or polluted, which aggravates the problem of water shortage. From the perspective mentioned above, it is also noteworthy to address water scarcity as one of the major global challenges in the 21st century [3]. Water scarcity is a combined effect of human-made and natural phenomenon, which affects every continent and has a direct impact on the ecosystem and human life [4]. As projected by the World Water Development Report 4, with the current consumption rate, around 1800 Million people throughout the world, will be facing total water scarcity by 2025. Furthermore, the remaining two-thirds of the world's population is expected to approach a physical water scarcity [5]. Shortly, the water resources are expected to face huge pressure to fulfil global water demands.

Membrane processes is a developed technology, which can address the challenges of water scarcity for being able to treat a wide range of water and wastewater and produce potable water of high quality [1]. The membrane technology can be customized easily, which increases the versatility and capacity of the technology for various applications [1, 6]. The most popular polymers for the fabrication of membranes are cellulose acetate (CA) [7], polyvinyl chloride (PVC) [8], polyvinyl alcohol (PVA) [9], polystyrene [10], polyvinylidene fluoride (PVDF) [11], polyacrylonitrile (PAN) [12], polyethersulfone (PES) [13] and polysulfone (PSf) [14]. It is noted that PSf is widely used due to its toughness, stiffness, stability at a higher temperature, and excellent film-forming properties [15]. Pristine PSf membranes are hydrophobic, which promotes severe fouling due to which the pure water flux decreases over time. Numerous efforts were made to decrease the fouling and overcome problems like poor water flux and low hydrophilicity of PSf membranes using hydrophilic additives, chemical grafting, and surface modification [16, 17]. Blending with hydrophilic additives attracted great attention due to the simplicity of the fabrication method via the non-solvent induced phase separation method. Hydrophilic additives are used as a

pore-forming agent to reduce the mass transfer resistance. Therefore, optimal pore size and uniform pore size distribution are required for ideal polymeric membranes.

Recently, the permeability and selectivity of the polymeric membranes are tuned using numerous polar additives such as inorganic nanoparticles, hydrophilic copolymers, and macromolecules [18]. The additives mentioned above change the viscosity of casting solution; as a result, the kinetics and thermodynamics of non-solvent induced phase separation have a significant impact on the membrane properties [19]. Several attempts were made to prepare blended membranes using iso-dimensional nanoparticles (SiO_2, TiO_2, Fe_3O_4, etc.) [20], one-dimensional nanoparticles (MWCNT, SWCNT, etc.) [21], two-dimensional materials (Clay, GO, rGO, WS_2, MoS_2, etc.) [22-24] and zero-dimensional quantum dots [25] to optimize the permeability and selectivity of membranes. Also, adding micro and nanofillers is the current promising trend for the preparation of composite and mixed matrix membranes [12]. Hence, an attempt has been made using a foremost budgetary, environmentally friendly, and easily available additive to enhance perm-selectivity and anti-fouling properties.

A decrease in the surface roughness with the enhanced polarity of the membrane protects the membrane surface from fouling caused by proteins and bacteria [26]. Biocidal polymers [27, 28] and metal ions [14, 29, 30] are also explored with various nanoparticles as a mitigation technique to avoid fouling of the membrane. However, poor interfacial compatibility of the inorganic nanomaterials results in its gradual detachment from the membrane surface and hence decreasing the membrane selectivity [31, 32] and increasing the fouling propensity of the membrane [31]. Change in the size of nanoparticles can further enhance interfacial compatibility. However, it would lead to the loss of inherent material properties [33]. Recent studies, therefore, are focused on the development of organic additives for the preparation of efficient membranes [34, 35].

Vanillin is the major flavor component of vanilla, and the presence of different functional groups such as alcohol, aldehyde, and ether in this aromatic compound attracted great attention [36].

Recently, Esmaeili Mohammadamin and co-workers [37] performed an antifouling study using vanillin with PES membrane for the treatment of wood originated streams. The study focused on the doping of water content with the PES solution, and vanillin was added to increase the membrane hydrophilicity. The study concluded that vanillin additive did increase not only the hydrophilicity of the PES membrane but also improved its antifouling properties. However, the study did not optimize the concentration of vanillin in the membrane, and the performance of the membrane was not compared with existing commercial membranes.

The present work, suggested vanillin to enhance the hydrophilicity, antifouling properties and to impart pores to the hydrophobic PSf membranes. Additionally, vanillin enhances the interconnectivity between pores and imparts multifunctional effects due to its chemical nature. It also improves the membrane morphology by accelerating the process of phase inversion, which results in the enhancement of performance studies. The vanillin is soluble in 1-Methyl-2-pyrrolidone (NMP) and deionized water. Blending water-soluble vanillin with PSf reduces the chemical-potential difference between the PSf-vanillin casting solution and DI water in the coagulation bath to achieve high water permeability. Flat sheet PSf-vanillin membranes with different vanillin concentration were fabricated to optimize the water permeability and rejection rate. The antifouling performance of PSf-vanillin membranes was investigated using bovine serum albumin (BSA) as model protein foulant. The rejection rate of fabricated membranes was tested using NaCl and $MgSO_4$ salts at constant 5 bar pressure. Finally, both antifouling and separation performance was compared with the commercially available TRISEP® UA60 nanofiltration membrane.

2. Experimental

2.1. Chemicals and materials

Polysulfone (PSf) (**Figure 1**) with an average molecular weight of 35kDa and 1-Methyl-2-pyrrolidone (NMP, > 99.5) were purchased from Sigma-Aldrich for membrane fabrication. Bovine

serum albumin (BSA) used for antifouling studies and 4-Hydroxy-3-methoxybenzaldehyde (Vanillin, Lot # BCCB4334) were obtained from Merck. Sodium chloride (NaCl), magnesium chloride ($MgSO_4$) used for the performance studies were supplied by Chem-supply, Australia. Deionized (DI) water obtained from Milli-Q®, Merck was used throughout the experiments to prepare a coagulation bath and to prepare diluted NaCl, $MgSO_4$, and BSA solutions. All the chemicals mentioned above were used as received. A commercial nanofiltration membrane TRISEP® UA60 used for comparison studies was purchased from MICRODYNADIR (A MANN+HUMMEL Company). Additional information about TRISEP® UA60 is provided in table 1. UA60 membrane was selected for fouling experiments because it is widely used in food processing, dairy filtration and wastewater treatment.

Table 1: TRISEP® UA60 membrane characteristics

Membrane	**UA60**	**PSf-vanillin**
Membrane material	Piperazine-based thin-film composite membrane	PSf-vanillin based composite membrane
Membrane module	Flat sheet	Flat sheet
Membrane thickness (μm)	130 - 170	83 - 97
Pore size distribution (Daltons)	1000	NA
Stabilized $MgSO_4$ Rejection (%)	80	57.85 – 87.49
NaCl Rejection (%)	10	9.58 – 25.78
Maximum Operating Pressure	41 bar (600 psi)	5 bar (72.51 psi) (Tested Pressure)
Maximum Operating Temperature	45°C (113°F)	~25 °C (Tested Temperature)

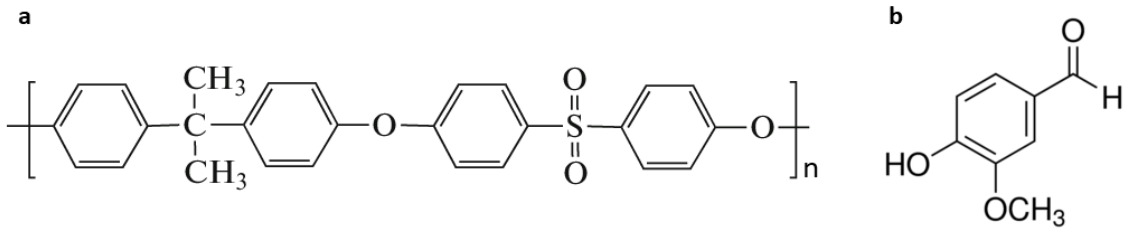

Figure 1: Molecular structure of polysulfone (a) and vanillin (b).

2.2. Membrane fabrication

PSf-vanillin composite membranes were fabricated using a non-solvent induced phase separation method, where PSf was used as a bulk polymeric material, NMP as a solvent, and vanillin as an additive. DI water was used as a non-solvent in the coagulation bath to obtain PSf-vanillin composite membranes (**Figure 2**). **Table 2** shows the composition of the casting solutions used for membrane fabrication. Initially, vanillin was dissolved using NMP for 1 hour at 60 °C, followed by PSf was added and stirred for 24 hours at the same temperature to obtain a homogeneous solution. The casting solutions were degasified for an hour before casting on the glass plate. Finally, a 200 µm casting knife was used to cast and transfer the membrane solution into a coagulation bath at 24 °C. The PSf-vanillin membranes were immersed in a DI water overnight before use to obtain mechanical stability. Notably, the casting solution was not homogeneous at vanillin concentration more than 30%.

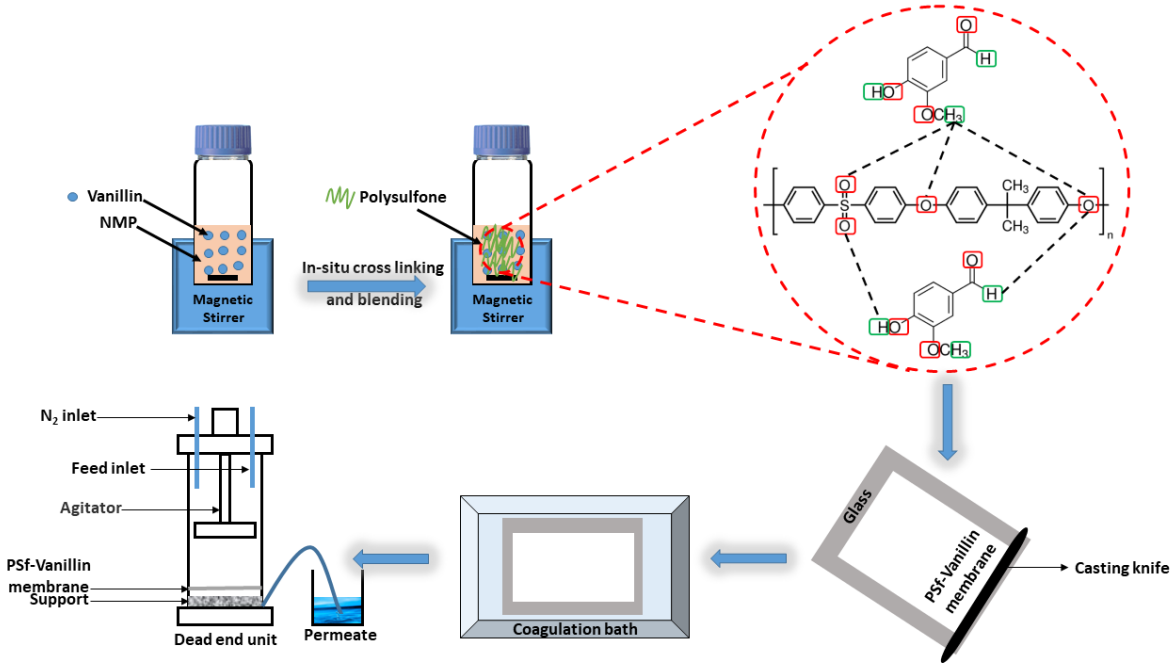

Figure 2: Schematic representation of the PSf-vanillin membrane fabrication process by in-situ cross-linking and blending.

Table 2: Composition of the casting solution for PSf-vanillin membranes.

Membrane	PSf (g)	NMP (mL)	Vanillin (g)
M_0	4	16	0
M_1	3.6	16	0.4
M_2	3.2	16	0.8
M_3	2.8	16	1.2

2.3. Membrane characterization

The PSf-vanillin membranes were dried completely using a vacuum oven to remove the water and moisture from membranes. Surface charge and chemistry, hydrophilicity, and structure parameters of the PSf-vanillin membranes were analyzed.

2.3.1. Physiochemical characterization

Functional group and cross-linking analysis of the membranes were investigated using Perkin Elmer Fourier transform infrared spectroscopy (FT-IR) spectra in the range of 500-4000 cm^{-1}. Surface zeta potential (Malvern) measurements were conducted to measure the surface charge of the membranes. The hydrophilicity of the PSf-vanillin composite membranes was analyzed using water uptake and contact angle measurements. Membrane samples with an active surface area of 2 × 2 cm^2 of were allowed for swelling in DI water for 24 hours at room temperature (~24°C ±2). The weight of the membrane was measured before (W_d) and after the swelling test (W_w). Finally, water uptake was measured using equation 1.

$$Water\ uptake = \frac{(W_w - W_d)}{W_d} \times 100 \quad (1)$$

The water contact angle was measured using the sessile drop method at five different locations for each membrane.

2.3.2. Structural characterization

2.3.2.1. Morphology

Cross-sectional and surface morphology were obtained using a field emission scanning electron microscope (FESEM). The cross-section samples were prepared using the freeze-fracturing method. Before scanning, the membrane surface was coated with a thin conductive film.

2.3.2.2. Overall membrane porosity and mean pore radius

The membrane porosity ε was defined as the volume of pores divided by the total volume of the porous membrane, i.e. the ratio between the volume of pores and that of pores + polymer. The overall porosity was thus calculated using equation 2 [38]:

$$\varepsilon = \frac{\frac{w_{wet} - w_{dry}}{\rho_w}}{\frac{w_{wet} - w_{dry}}{\rho_w} + \frac{w_{dry}}{\rho_p}} \quad (2)$$

where ε is the overall porosity of the membrane (%), w_{wet} and w_{dry} the weights of wet and dry membrane (g), ρ_w and ρ_p the densities of water and polymer (g/cm^3). Wet and dry weights were determined by the gravimetric method. Membranes (1 cm²) were first immersed in DI water for 24 hours, then wet membranes were weighted after wiping excessive water on the surfaces with filter paper. Finally, the membranes were dried in a vacuum oven at 60 °C for 24 h before being weighted.

The overall membrane pore radii (r_m) were calculated from pure water flux and porosity values with the Guerout-Elford-Ferry equation [39]:

$$r_m = \sqrt{\frac{(2.9-1.75\varepsilon)\ 8\ \eta\ L\ Q}{\varepsilon\ A\ \Delta P}} \quad (3)$$

Where L and A are the membrane thickness and area, η the water viscosity (8.9×10^{-4} Pa s), and Q the permeate flow at an applied pressure ΔP.

2.3.2.3. Mean pore radius of the skin layer

The performance of filtration tests are mostly governed by the properties of the skin layer. For this reason, overall values, which take the properties of all the membrane layers into account, is not necessarily relevant to discuss performances. For this reason, the mean pore radius was estimated by fitting salt rejection with a usual transport model based on the coupling between Steric and Donnan exclusion at the pore/solution interfaces (equation 4) and the extended Nernst-Planck equation (equation 5) for transport description. This model was previously accurately detailed in other works [40, 41].

$$\frac{c_i}{c_i} = \phi_i \exp\left(\frac{-z_i F}{RT}\Delta\psi_D\right) \quad (4)$$

where $\Delta\psi_D$ is the Donnan potential and ϕ_i the steric partitioning coefficient calculated from the ion Stokes radius r_i and mean pore radius r_p by $\phi_i = \left(1 - \frac{r_i}{r_p}\right)^2$.

$$j_i = K_{i,d} D_{i,\infty} \frac{dc_i}{dx} - \frac{z_i\, c_i\, K_{i,d}\, D_{i,\infty}}{R\,T}\, F\, \frac{d\psi}{dx} + K_{i,c}\, c_i\, V \quad (5)$$

Where, $D_{i,\infty}$, z_i and c_i are the diffusivity at infinite dilution, the valence, and the local concentration of ion i, respectively. V and ψ are the velocity inside pores and the electric potential. Equation 5 also includes hindrance factors for convection $K_{i,c}$ and diffusion $K_{i,d}$ for which calculations have already been detailed in other works [40, 42].

It should be mention that dielectric exclusion was not considered in this application. With this approach, the filtration performances can be fitted using three input parameters:

- the intrinsic membrane permeability L_p, which can be easily calculated from pure water flux J_w with Darcy's law (Eq. 6):

$$L_p = \frac{J_w\, \eta}{\Delta P} \quad (6)$$

- the volumetric membrane charge X_d, which was estimated from ζ-potential values considering the Gouy–Chapman theory for cylindrical pores, with Eq. 7 [43, 44]:

$$X_d = \frac{2sign(\varsigma)\sqrt{\left(2\varepsilon_0\varepsilon_b RT \sum_i C_i\left[exp\left(\frac{-z_i F\varsigma}{RT}\right)-1\right]\right)}}{F r_p} \quad (7)$$

- the mean pore radius r_p, which was numerically adjusted to fit experimental salt rejection.

2.4. Performance studies

Filtration tests were performed using HP4750 dead-end setup provided by Sterlitech Company (USA) with an active membrane surface area 14.6 cm^2, processing volume 300 mL at constant 5 bar pressure. All membranes were compacted for an hour before taking initial readings with DI water as feed at constant 5 bar pressure to achieve a steady permeate state before characterization.

2.4.1. Pure water flux

Water flux studies were carried out using the Sterlitech HP4750 dead-end unit at a constant pressure of 5 bar provided from a nitrogen cylinder. After compaction, the permeate was collected for an hour at a constant interval of 10 minutes. Equation 8 was used to determine the pure water flux.

$$J_w = \frac{V}{A \times t} \tag{8}$$

Where J_w is the pure water flux in terms of L/(m^{2}h); V is the volume of permeate in litters (L); A is active membrane surface area in m^2 and t is the permeation time in hours (h).

2.4.2. Antifouling studies

The above-mentioned dead-end setup was used in the investigation of antifouling properties of the PSf and PSf-vanillin membranes with 200 mg/L BSA feed solution as a model foulant. Initially, pure water flux (J_1) was measured for 60 mins at 5 bar pressure (section 2.4.1.). Then, the dead-end unit was filled with the BSA feed solution, and permeate flux (J_P) was collected for an hour at10 mins time interval. Used membranes were washed thoroughly with DI water, and pure water flux (J_2) was calculated again to measure the decline in water flux. Flux recovery ratio (FRR) was calculated from equation 9:

$$FRR\ (\%) = \left(\frac{J_2}{J_1}\right) \times 100 \tag{9}$$

Reversible (R_r), irreversible (R_{ir}) and total fouling (R_t) was measured using equation 10-12, for a complete understanding of the fouling behaviour of the PSf-vanillin membranes.

$$R_r\ (\%) = \left(\frac{J_2 - J_P}{J_1}\right) \times 100 \tag{10}$$

$$R_{ir}\ (\%) = \left(\frac{J_1 - J_2}{J_1}\right) \times 100 \tag{11}$$

$$R_t\ (\%) = \left(1 - \frac{J_P}{J_1}\right) \times 100 \tag{12}$$

2.4.3. Filtration performances

The rejection rate of PSf and PSf-vanillin membrane was investigated using 2000 ppm $MgSO_4$, and NaCl solutions at 5 bar pressure and 24°C ± 2 feed temperature. The duration of salt rejection tests was 60 minutes, and water permeate was collected every 10 minutes. Each set of experiments was performed for three times, and the mean value was reported. A conductivity meter (LAQUA PC210) was used to determine the concentration of feed and permeate, while the rejection rate was calculated from equation 13. Permeate flux of salt solution was also measured every 10 mins by Eq. 8, in the same as pure water flux.

The rejection rate of BSA (200 mg/L) was investigated using a dead-end filtration unit. Here, prepared BSA solution was used as feed and stirred with the help of magnetic stirrer while the operation to minimize the effect of concentration polarization. The rejection rate was calculated according to equation 13:

$$Rejection\ (\%) = \left(1 - \frac{C_P}{C_f}\right) \times 100 \quad (13)$$

Where C_f is feed concentration, and C_P is the permeate concentration determined with the help of UV–Visible spectrophotometer.

3. Results and discussion

3.1. Surface functional group analysis

FT-IR spectra for vanillin, PSf, and PSf-vanillin membranes are shown in **Figure 3**. The stretching vibration for –OH was observed at 3152 cm^{-1} for vanillin. C-H stretching for methyl group present in vanillin shows a typical peak at 2856 cm^{-1}, C=O of aldehyde group at 1660 cm^{-1}. Benzene ring shows various stretching vibrations at 1585, 1508, and 812 cm^{-1} respectively. The phenolic hydroxyl group in vanillin shows the bending vibration peak at 1263 cm^{-1} [45]. Vanillin incorporated membranes show common peaks with pristine PSf membrane confirming polysulfone backbone structure. SO_2 groups of membranes show peaks at 1150 and 1295 cm^{-1}. C=C stretching at 1584 cm^{-1} and aromatic C-H bending at 833 cm^{-1} [16, 46]. As highlighted in

Figure 3, after the incorporation of vanillin with PSf, slight changes are observed for two peaks for PSf-vanillin membranes. Firstly, a slight shift of –OH stretching region (3100 -3600 cm^{-1}) in PSf-vanillin membranes is observed, which could be attributed to the formation of strong intermolecular hydrogen bonding between vanillin and PSf. Secondly, the changes (1550-1750 cm^{-1}) could be due to strong π - π interactions between aromatic rings of vanillin and PSf. A plausible mechanism for the formation of hydrogen bonding is shown in **Figure 4**.

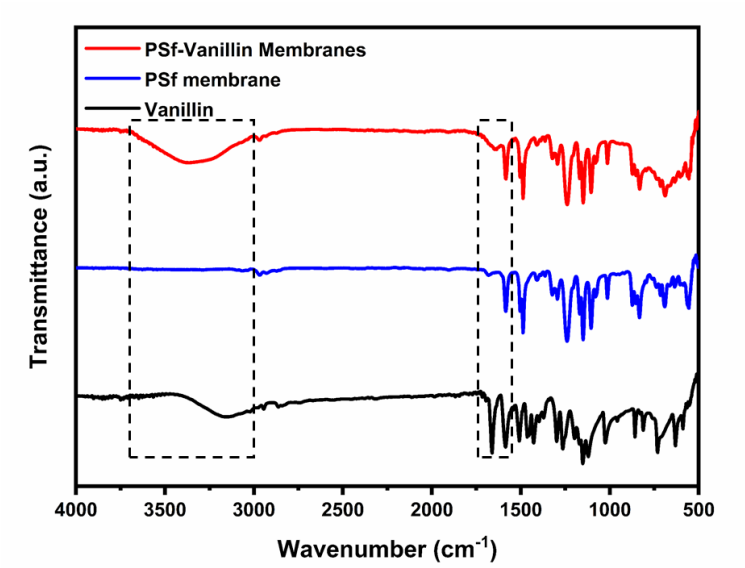

Figure 3: FT-IR for vanillin, PSf, and PSf-vanillin membranes

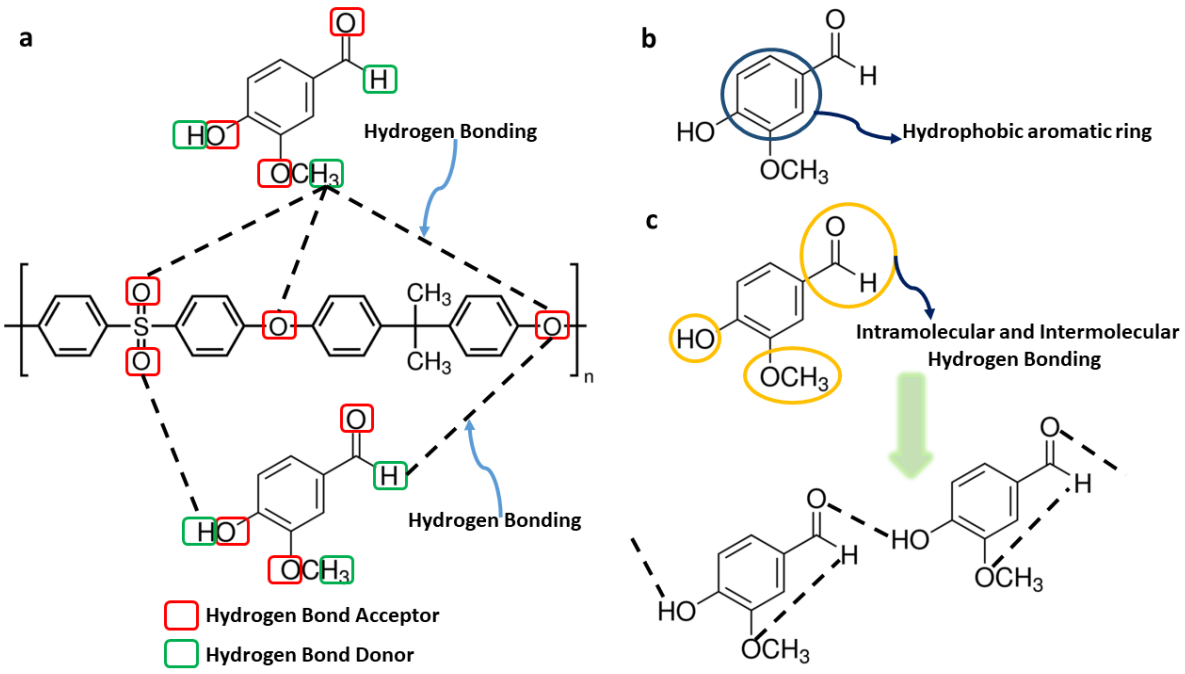

Figure 4: Possible intermolecular hydrogen bonding between vanillin and polysulfone moieties (a), hydrophobic aromatic ring of vanillin for π – π interactions with polysulfone (b) and Intramolecular hydrogen bonding between vanillin moieties (c)

3.2. Porosity and mean pore radius

Table 3 summarizes the structural properties, namely the membrane thickness L, the overall porosity ε estimated by gravimetric method, the overall membrane pore radius r_m estimated by the Guerout-Elford-Ferry equation and the mean pore radius r_p identified by fitting $MgSO_4$ rejections (provided in section 3.6.2).

Table 3: Structural properties of the various PSf-vanillin membranes.

Membrane	L (μm)	ε	r_m (nm)	r_p (nm)
M_1	97	46	5.6	0.6
M_2	95	53	7.3	0.55
M_3	83	61	9.2	0.7

Table 3 shows that the overall porosity of the membranes increases with the increase in vanillin content ($M_3 > M_2 > M_1$), even if it can be seen in Figure 5 that the volume of macropores (in the support layer) seems to be higher when vanillin content is low. This suggests that overall porosity is strongly governed by micro- and mesoporosity. It should be noted that this sequence of porosity seems to be confirmed by permeate flux provided hereafter (section 3.6.1).

These porosity values were then used to estimate the mean pore radius (by the Guerout-Elford-Ferry equation) and the same sequence was obtained ($M_3 > M_2 > M_1$). However, the relatively large sizes confirm that the latter is overall values mainly governed by mesoporosity of the various layers. To investigate only skin layer properties, mean pore radii of the three membranes were assessed by fitting $MgSO_4$ rejection values, knowing membrane charge (provided in **Figure** 7a).

The obtained pore sizes are typical of membranes on the boundary between nano- and tight ultrafiltration. From the identified values, it seems that the size of surface pores does not monotonously increase with vanillin content. However, the M_3 membrane exhibits the highest pore radius, which seems consistent with the FESEM images of the top surface (**Figure 5**).

3.3. Morphology of PSf-vanillin membranes

Figure 5 represents the morphology of the top surface (**a-d**), the bottom surface (**e-f**), and the cross-section surface (**i-l**) of membranes M_0, M_1, M_2, and M_3, respectively. The effect of loaded vanillin on the micro-structure of PSf membrane was analyzed. All membranes are asymmetric with porous support and a dense skin layer. With the addition of vanillin, more pores are observed at the bottom surface of the membrane, which confirms an increase in the porosity of the membranes from M_0 to M_3. Adding 30% vanillin to membrane M_3 showed an irregular top surface and minor cracks (**Figure 5d**), which is probably attributed to the change in the viscosity of the casting solution. In the PSf membrane, closed-end drop-like channels were observed (**Figure 5i**), due to which the PSf membrane showed almost a negligible pure water flux at 5 bar pressure. However, adding vanillin, long finger-like channels were observed, which led to an increase in the water permeability of membranes. Also, increasing the vanillin contents resulted in more pores on the bottom surface of the membrane. Images of cross-section and bottom surface confirm the formation of porous support in PSf-vanillin membranes. Presence of vanillin in the prepared membranes was confirmed using FT-IR. The FT-IR test confirms the cross-linking of vanillin with the PSf polymer (**Section 3.1.**). Increase in the solvent-nonsolvent exchange rate was observed during membrane fabrication which might be attributed to the solubility of vanillin in both water and the organic solvent used for membrane preparation [47, 48]. As a result, porous wall thickness between long fingers like channels are formed. The change in the microstructure of cross-section and bottom surface images compared to pristine PSf membrane could be attributed to the cross-linking between vanillin and PSf polymer. Also, there is a strong inter, and intramolecular

hydrogen bonding and π – π interactions between vanillin and PSf might also be possible, as shown in **Figure 4**.

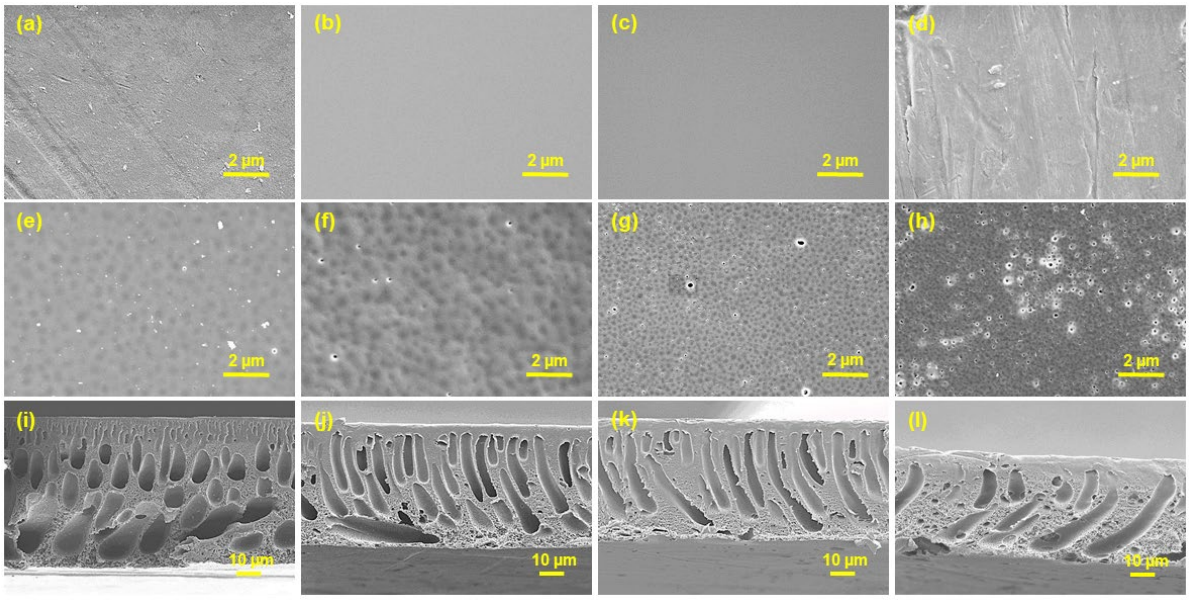

Figure 5: FESEM images of the top surface (a-M_0, b-M_1, c-M_2, and d-M_3), bottom surface (e-M_0, f-M_1, g-M_2, and h-M_3) and cross-section (i-M_0, j-M_1, k-M_2, and l-M_3) PSf-vanillin membrane surfaces.

3.4. Hydrophilicity

The hydrophilicity of the PSf-vanillin membranes was evaluated using water contact angle measurements, and corresponding results are shown in **Figure 6**. All the vanillin incorporated membranes show a lower water contact angle compared to the pristine PSf membrane (70.2°). Further, with the addition of a small amount of hydrophilic vanillin as an additive, the water contact angle reduces to 66.6°, 60.7°, and 53.7° for M1, M_2, and M_3 respectively. The water contact angle decreases with an increase in the degree of cross-linking between PSf and Vanillin moieties as confirmed with FT-IR. The results are in good agreement with the hydrophilicity measurement trend of hydrophilic additive blended membranes [49]. Also, the results of surface zeta potential measurements and water uptake reflected a similar trend.

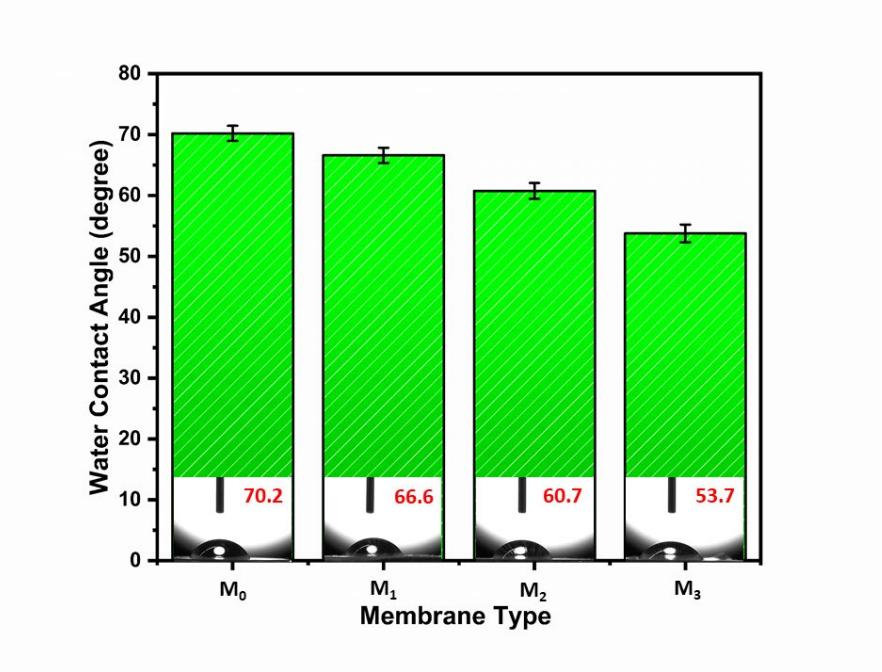

Figure 6: Water contact angle measurements for the PSf-vanillin membrane surfaces.

Water uptake is a key parameter for measuring the total water content and the hydrophilic properties of the PSf-vanillin membranes. Figure 7 shows the water uptake capacity of the membranes. Water uptake capacity of the membrane increased with increasing the concentration of vanillin, probably, due to the presence of polar functional groups on the surface, which increased the affinity of water to the surface of the membrane. Also, the increase in the water uptake capacity was due to the formation of a porous network, as illustrated in Figure 5. Thus, M_3 membrane showed the highest water uptake capacity of 123.6 ± 3.4, due to the presence of a highly porous network. In addition, the water uptake capacity of M_2 (92.5 ± 2.5), and M_1 (69.2 ± 3) was lower than that of M_3 membrane as they have less porous structure compared to M_3 membrane. The PSf M_1 membrane showed the lowest water uptake capacity due to its hydrophobic nature and closed-end drop-like non-porous cross-sectional morphology (Figure 5i).

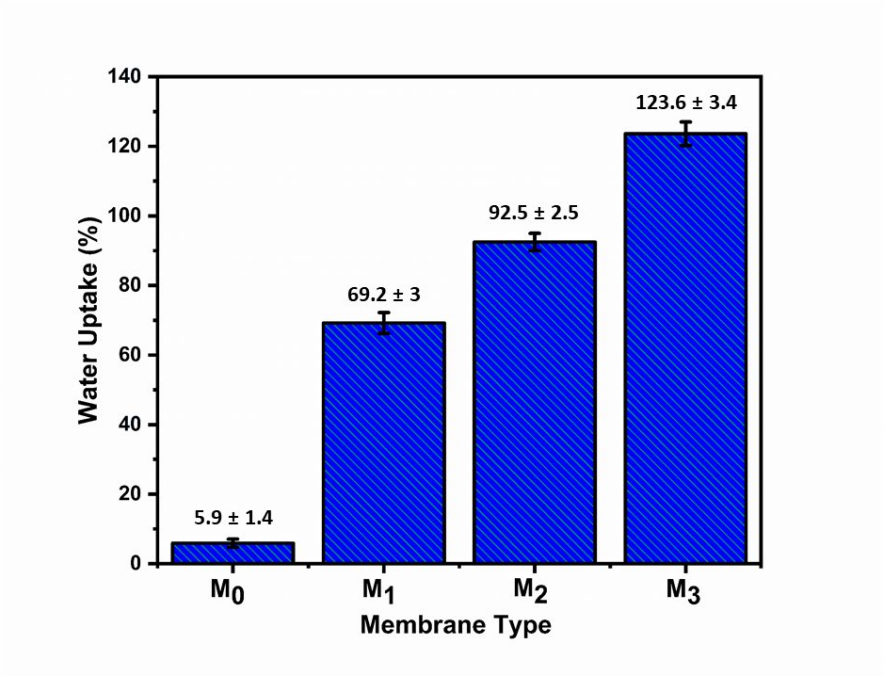

Figure 7: Water uptake studies for the PSf-vanillin membranes.

3.5. Surface charge and thermal stability

Surface zeta potential measurements for PSf-vanillin membranes are presented in **Figure 8a**. As shown, all the membranes showed negative values with an increase in the vanillin loading negative charge increases. In general, zeta potential plays an important role in permeability and anti-fouling performance of membranes [50]. The negative surface charge on the PSf-vanillin membranes is the indication of the presence of charged polar functional group on the membrane surface [51]. During membrane solidification, hydrophilic vanillin migrates to the top surface, and as a result, negative zeta potential is observed. Also, with an increase in the polar functional groups on the surface helps in the reduction of interface energy with water [52]. Hydrophilic vanillin helps in the enhancement of the solvent-nonsolvent exchange rate, which helps in the formation of the porous support. The porous network enhances the permeability of the membrane by reducing the mass transfer resistance.

For all the PSf-vanillin membranes thermal stability is as important as hydrophilicity, permeability, and selectivity for industrial applications. Thermal stability is evaluated for all the

PSf-vanillin membranes, and thermograms are shown in **Figure 8b**. PSf based membranes show the decomposition temperature for the polymeric chain around 500°C [16, 46]. With an increase in the vanillin concentration, a slight decrease in thermal stability is observed. There are three main stages of the weight loss for the membranes. Initially, weight loss is observed from 90°C to 130°C. This weight reduction is attributed to the loss of water molecules attached or present on the hydrophilic surface of membranes [53]. Secondly, the weight reduction is observed in the range of 150°C to 450°C, which is assigned the removal of various functional present in the vanillin. Lastly, PSf backbone degrades above 450°C. In M_3 membrane as few cracks are observed on the top and bottom surface in FESEM images (**Figure 5**), due to which weight loss is higher compare to other membranes. To conclude, the PSf-vanillin membranes shows good thermal stability.

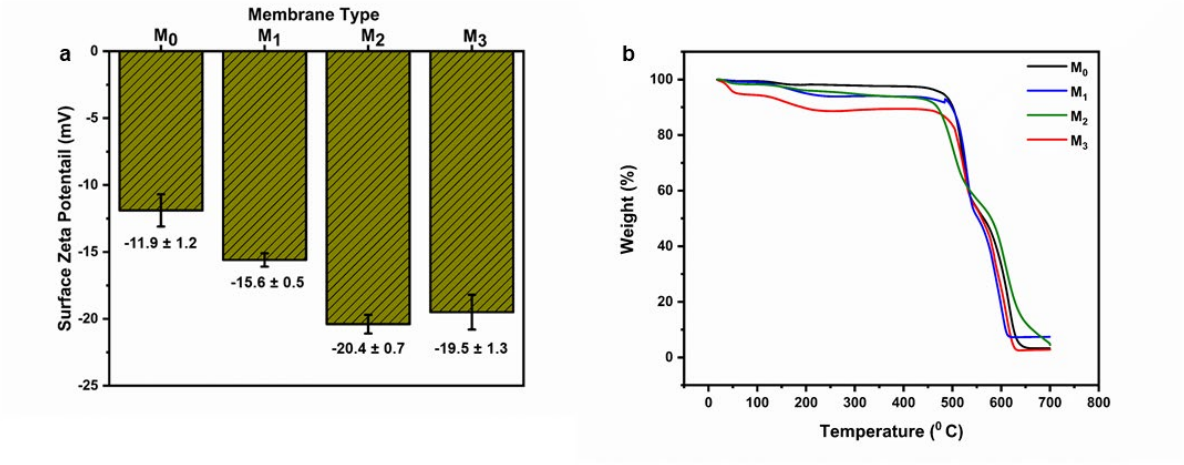

Figure 8: a) Surface zeta potential measurement for the PSf-vanillin membranes, b) Thermal stability for the PSf-vanillin membranes.

3.6. Filtration performances

3.6.1. Pure water flux

Pure water flux performance was calculated using the dead-end unit at constant 5 bar pressure and DI water feed solution and results compared with a NADIR nanofiltration membrane UA60 (**Figure 9**). The ratio of PSf to vanillin plays a significant role in determining the porous structure

and water permeability of the membrane. Experimental work revealed that the pure water flux was 87.18, 75.94, 39.84, and 20.015 LMH for M_3, UA60, M_2, and M_1 membrane, respectively. The highest water flux was achieved in membrane M3, which contains the highest ration of vanillin to PSf. The hydrophilicity of membranes M_1 to M_3 was achieved by the inclusion of vanillin moieties (Figure 3), which also maintained the formation of membranes porous network (Figure 5). As a result, increasing the vanillin ratio increased the pure water flux. Similarly, the presence of polar hydroxyl (-OH) and aldehyde (-CHO) functional groups, which were imparted by vanillin, helped to capture water molecules on the surface of the membranes.

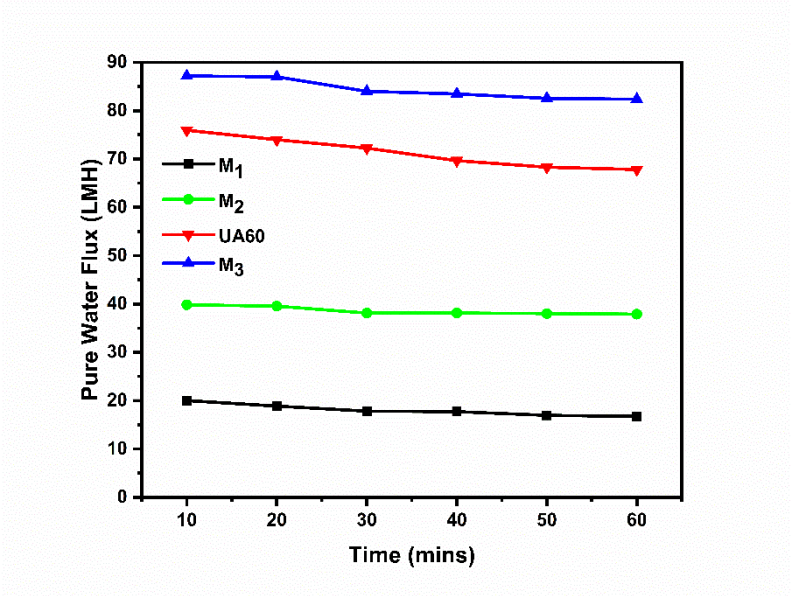

Figure 9: Pure water flux measurements for the PSf-vanillin membranes.

3.6.2. Salt Rejection (NaCl and $MgSO_4$)

A dead-end filtration process was performed to evaluate salt rejection for the PSf-vanillin membranes and the commercial membrane UA60. **Figure 10a** and **10b** show a steady-state water flux performance of the PSf-vanillin membranes and the commercial membrane UA60 using 2000 ppm $MgSO_4$ and NaCl feed solution. Table 4 shows the rejection rate of PSf-vanillin and the commercial membrane UA60. It can be observed that permeate flux increased more than five-fold (from 15.18 LMH for membrane M_1 to 81.45 LMH for membrane M_3) with the increase in the

vanillin concentration from 10% to 30%. Water flux increased with an increase in the hydrophilicity of the membranes from M_1 to M_3. Also, the increase in the water flux stimulates convection of salt molecules through the membrane, as a result of decreasing in the salt rejection was observed up to 57.85 for $MgSO_4$ and 9.58 for NaCl for M_3 membrane. Compared to the M2 membrane, M1 membrane has slightly lower salt rejection due to its lower negative surface charge. The decline in salt rejection was not as sharp as in the case of permeate flux. Membrane M_2 shows the highest salt rejection of 87.49% for $MgSO_4$ and 25.78% for NaCl solution. Comparing to membrane UA60, M_2 membrane showed ~10% higher rejection for $MgSO_4$ and 15% increase for the NaCl rejection. Although the water flux was slightly lower, membrane M_2 showed better salt rejection performance. PSf-vanillin membranes showed better rejection of $MgSO_4$ compared with the NaCl (Figure 11a and 11b). This phenomenon could be explained by the Donnan effect, where divalent anions (such as SO_4^{-2}) are more rejected than monovalent anions (such as Cl^{-1}) by a negatively charged membrane [54]. The results are in good agreement with surface charge, wettability and hydrophilicity of the PSf-vanillin membranes.

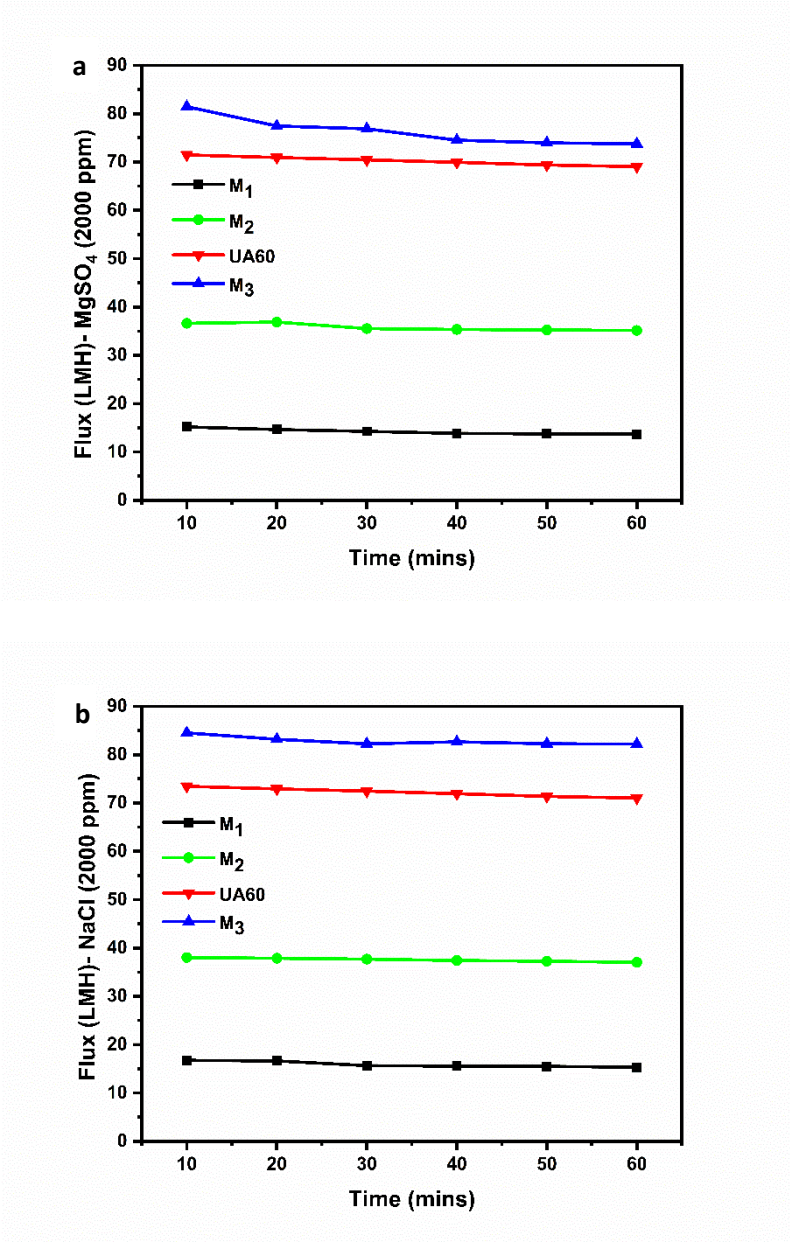

Figure 10: Permeate flux obtained for NaCl (a) and $MgSO_4$ (b) solutions with the PSf-vanillin membranes and the commercial UA60 membrane.

Table 4: $MgSO_4$ and NaCl rejection performance for the PSf-vanillin membranes and commercial UA60 membrane.

Membrane	$MgSO_4$ Rejection (%)	NaCl Rejection (%)
M_1	75.46 ± 1.67	21.98 ± 2.33
M_2	87.49 ± 2.03	25.78 ± 2.41

M_3	57.85 ± 2.67	9.58 ± 3.65
UA60	77.13 ± 3.12	12.02 ± 2.94

3.6.3. Antifouling properties

Fouling is one of the major challenges facing membrane processes and deteriorates its performance [55]. The incorporation of PSf-vanillin will increase the hydrophilic character of the membrane, and hence the antifouling properties of the membrane are expected to enhance. To investigate the membrane antifouling capabilities, BSA solution was used as a model foulant. **Figure 11** shows the flux for DI water and BSA. A sharp decline of water flux was observed when BSA was added to the feed solution (**Figure 11**). Compared to the modified membranes, a substantial decline of permeate flux is observed for the commercial UA60 membrane (75.9 LMH to 38.63 LMH). The lowest decline of water flux was 52% for membrane M_1 (20.01 LMH to 9.6 LMH), followed by 33% for membrane M_2 (39.2 LMH to 26.36) and 17% for membrane M_3 (86.9 LMH to 72.22 LMH) membranes respectively. This rapid flux decline can be attributed to the BSA adsorption and pore blockage (less probable). After the filtration performance test, the fouled membrane was cleaned with DI water to assess the recovery of the water flux of the fouled membranes. The mechanism of BSA fouling is complex and due to two main mechanisms, i.e. i) deposition of BSA aggregates on the membrane surface and, ii) chemical attachment to the deposited BSA[56, 57].

A high water restoration rate was observed for PSf-vanillin membranes after physical cleaning with DI water. Notably, membranes M_2 and M_3 show the highest water flux recovery ratio (FRR) with 88.55% and 90.02% respectively followed by 84.02% FRR for the commercial UA60 membrane and 73.24% for the membrane M_1 (**Figure 12a)**. The rejection rate of BSA was around 99.9% for membranes M_2 and commercial UA60. A slight decline for BSA rejection is observed in the case of M_3 membrane, which might be due to the formation of a vast porous network (**Figure 5**).

Membrane fouling due to pore blocking is usually irreversible and difficult to remove by physical cleaning even by strong shear forces. However, reversible fouling caused due to the cake layer or gel layer can be removed by simple physical cleaning and is known as reversible fouling. The anti-fouling properties were analyzed for all the PSf-vanillin membranes, and the results were compared with the commercial membrane UA60. Figure 10c shows the reversible fouling (R_r), irreversible fouling (R_{ir}), and total fouling (R_t). The higher total fouling was 52.1% in membrane M_1 and 49.2% for the commercial membrane UA60. Notably, the M_2 and M_3 membrane show 33.9% and 17.2% total fouling respectively. **Figure 12b** clearly shows that the PSf-vanillin membrane has better antifouling properties, which are attributed to the following reasons:

a) PSf-vanillin membranes are highly hydrophilic, which weakened the interactions between the membrane surface and BSA foulant.

b) The negative surface charge of the PSf-vanillin membranes increased the electrostatic repulsion between negatively charged BSA foulant and the surface of the PSf-vanillin membrane.

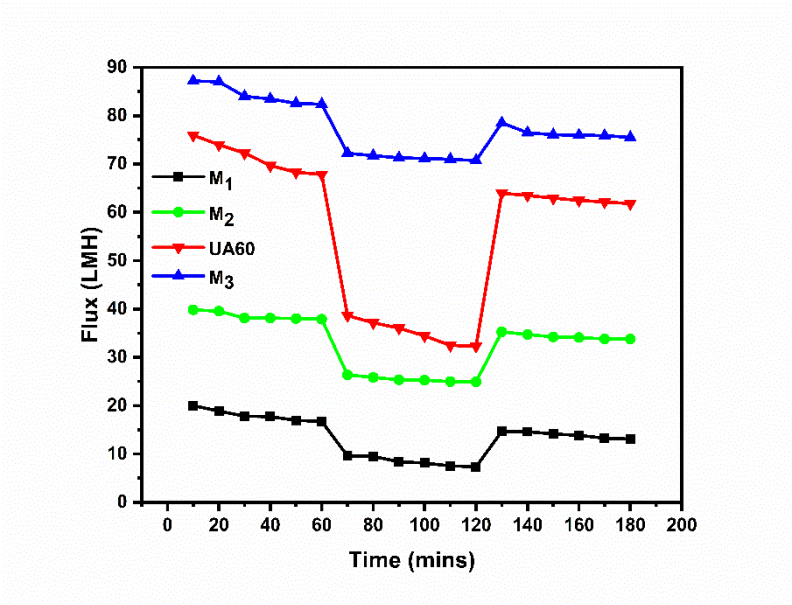

Figure 11: Pure water flux and BSA solution water flux measurements for the PSf-vanillin membranes and commercial UA60 membrane.

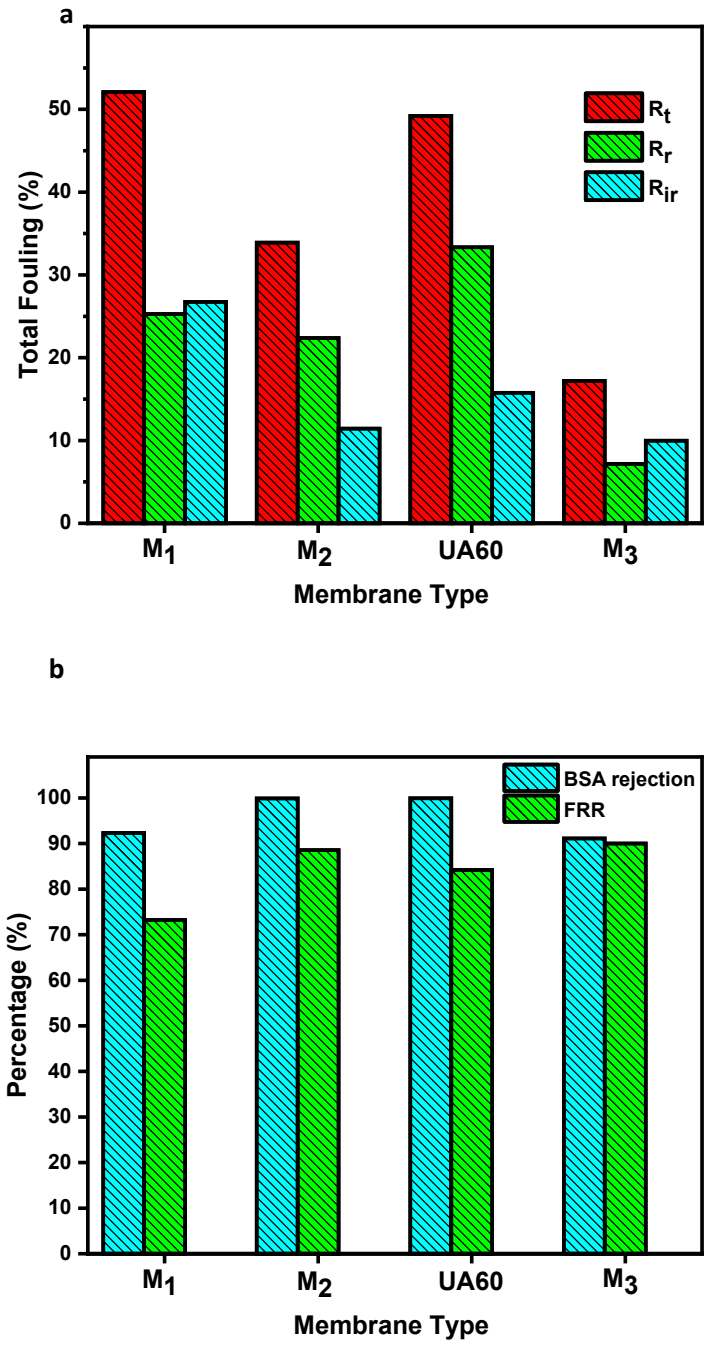

Figure 12: Total fouling, reversible fouling and irreversible fouling (a) and FRR and BSA rejection percentage (b) for the PSf-vanillin membranes and commercial UA60 membrane.

4. Conclusion

The present work elaborates on the fabrication, characterization, antifouling and salt rejection performance of a novel environmental friendly vanillin incorporated PSf based nanofiltration

membranes. Incorporation of vanillin in PSf based casting solution imparts porosity and sufficient negative surface charge to display 87.49% and 25.78% rejection of $MgSO_4$ and NaCl while maintaining high permeate flux of 36-38 LMH at constant 5 bar pressure. The rejection mechanism for $MgSO_4$ and NaCl can be identified as strong negative-negative charge repulsion between the membrane surface and negative SO^{-2} and Cl^- ions. The PSf-vanillin membranes have similar permeate flux to ultrafiltration membranes and $MgSO_4$ and NaCl rejection to nanofiltration membranes. In addition, PSf-vanillin membranes shows several distinguished features like very low fouling with better flux recovery ratio up to 88.55% and cost-effective. Taking into the account the benefits mentioned above, PSf-vanillin membranes to have techno-commercial applicability for the treatment of low-quality wastewaters and industrial wastewater.

Acknowledgement

The findings achieved herein are solely the responsibility of the authors. PhD candidate Sudesh Yadav would like to acknowledge scholarship support from University of Technology Sydney under UTS President's Scholarship and International Research Scholarship (IRP).

References

[1] S. Yadav, H. Saleem, I. Ibrar, O. Naji, A.A. Hawari, A.A. Alanezi, S.J. Zaidi, A. Altaee, J. Zhou, Recent developments in forward osmosis membranes using carbon-based nanomaterials, Desalination, 482 (2020) 114375.
[2] S. Yadav, I. Ibrar, S. Bakly, D. Khanafer, A. Altaee, V. Padmanaban, A.K. Samal, A.H. Hawari, Organic Fouling in Forward Osmosis: A Comprehensive Review, Water, 12 (2020) 1505.
[3] P. Greve, T. Kahil, J. Mochizuki, T. Schinko, Y. Satoh, P. Burek, G. Fischer, S. Tramberend, R. Burtscher, S. Langan, Global assessment of water challenges under uncertainty in water scarcity projections, Nature Sustainability, 1 (2018) 486-494.
[4] R. Nair, H. Wu, P. Jayaram, I. Grigorieva, A. Geim, Unimpeded permeation of water through helium-leak–tight graphene-based membranes, Science, 335 (2012) 442-444.
[5] R. Connor, The United Nations world water development report 2015: water for a sustainable world, UNESCO publishing, 2015.
[6] A.G. Fane, R. Wang, M.X. Hu, Synthetic membranes for water purification: status and future, Angewandte Chemie International Edition, 54 (2015) 3368-3386.

[7] S. Yang, Q. Zou, T. Wang, L. Zhang, Effects of GO and MOF@ GO on the permeation and antifouling properties of cellulose acetate ultrafiltration membrane, Journal of membrane science, 569 (2019) 48-59.
[8] M. Yong, Y. Zhang, S. Sun, W. Liu, Properties of polyvinyl chloride (PVC) ultrafiltration membrane improved by lignin: Hydrophilicity and antifouling, Journal of membrane science, 575 (2019) 50-59.
[9] A.K. Thakur, S.P. Singh, M.c.N. Kleinberg, A. Gupta, C.J. Arnusch, Laser-Induced Graphene–PVA Composites as Robust Electrically Conductive Water Treatment Membranes, ACS applied materials & interfaces, 11 (2019) 10914-10921.
[10] S. Parakala, S. Moulik, S. Sridhar, Effective separation of methylene blue dye from aqueous solutions by integration of micellar enhanced ultrafiltration with vacuum membrane distillation, Chemical Engineering Journal, 375 (2019) 122015.
[11] X.-T. Yuan, C.-X. Xu, H.-Z. Geng, Q. Ji, L. Wang, B. He, Y. Jiang, J. Kong, J. Li, Multifunctional PVDF/CNT/GO mixed matrix membranes for ultrafiltration and fouling detection, Journal of hazardous materials, 384 (2020) 120978.
[12] P.H. Duong, V.A. Kuehl, B. Mastorovich, J.O. Hoberg, B.A. Parkinson, K.D. Li-Oakey, Carboxyl-functionalized covalent organic framework as a two-dimensional nanofiller for mixed-matrix ultrafiltration membranes, Journal of membrane science, 574 (2019) 338-348.
[13] L. Zverina, M. Koch, M.F. Andersen, M. Pinelo, J.M. Woodley, A.E. Daugaard, Controlled pore collapse to increase solute rejection of modified PES membranes, Journal of Membrane Science, 595 (2020) 117515.
[14] K. Sunil, G. Karunakaran, S. Yadav, M. Padaki, V. Zadorozhnyy, R.K. Pai, Al-Ti2O6 a mixed metal oxide based composite membrane: A unique membrane for removal of heavy metals, Chemical Engineering Journal, 348 (2018) 678-684.
[15] D. Emadzadeh, W.J. Lau, T. Matsuura, M. Rahbari-Sisakht, A.F. Ismail, A novel thin film composite forward osmosis membrane prepared from PSf–TiO2 nanocomposite substrate for water desalination, Chemical Engineering Journal, 237 (2014) 70-80.
[16] S. Yadav, K. Soontarapa, M. Jyothi, M. Padaki, R.G. Balakrishna, J.-Y. Lai, Supplementing multifunctional groups to polysulfone membranes using Azadirachta indica leaves powder for effective and highly selective acid recovery, Journal of hazardous materials, 369 (2019) 1-8.
[17] M. He, T. Li, M. Hu, C. Chen, B. Liu, J. Crittenden, L.-Y. Chu, H.Y. Ng, Performance improvement for thin-film composite nanofiltration membranes prepared on PSf/PSf-g-PEG blended substrates, Separation and Purification Technology, 230 (2020) 115855.
[18] L.Y. Ng, A.W. Mohammad, C.P. Leo, N. Hilal, Polymeric membranes incorporated with metal/metal oxide nanoparticles: a comprehensive review, Desalination, 308 (2013) 15-33.
[19] M. Mulder, Basic principles of membrane technology, Springer Science & Business Media, 2012.
[20] C. Wolf, H. Angellier-Coussy, N. Gontard, F. Doghieri, V. Guillard, How the shape of fillers affects the barrier properties of polymer/non-porous particles nanocomposites: A review, Journal of Membrane Science, 556 (2018) 393-418.
[21] S. Majeed, D. Fierro, K. Buhr, J. Wind, B. Du, A. Boschetti-de-Fierro, V. Abetz, Multi-walled carbon nanotubes (MWCNTs) mixed polyacrylonitrile (PAN) ultrafiltration membranes, Journal of Membrane Science, 403 (2012) 101-109.
[22] G. Liu, W. Jin, N. Xu, Graphene-based membranes, Chemical Society Reviews, 44 (2015) 5016-5030.
[23] H.-H. Huang, R.K. Joshi, K.K.H. De Silva, R. Badam, M. Yoshimura, Fabrication of reduced graphene oxide membranes for water desalination, Journal of membrane science, 572 (2019) 12-19.
[24] S. Yadav, I. Ibrar, A. Altaee, A.K. Samal, R. Ghobadi, J. Zhou, Feasibility of brackish water and landfill leachate treatment by GO/MoS2-PVA composite membranes, Science of The Total Environment, (2020) 141088.
[25] Z. Zeng, D. Yu, Z. He, J. Liu, F.-X. Xiao, Y. Zhang, R. Wang, D. Bhattacharyya, T.T.Y. Tan, Graphene oxide quantum dots covalently functionalized PVDF membrane with significantly-enhanced bactericidal and antibiofouling performances, Scientific reports, 6 (2016) 20142.

[26] C. Parra, F. Montero-Silva, R. Henríquez, M. Flores, C. Garín, C. Ramírez, M. Moreno, J. Correa, M. Seeger, P. Häberle, Suppressing bacterial interaction with copper surfaces through graphene and hexagonal-boron nitride coatings, ACS applied materials & interfaces, 7 (2015) 6430-6437.
[27] X. Zhao, Y. Su, Y. Li, R. Zhang, J. Zhao, Z. Jiang, Engineering amphiphilic membrane surfaces based on PEO and PDMS segments for improved antifouling performances, Journal of membrane science, 450 (2014) 111-123.
[28] X. Chen, G. Zhang, Q. Zhang, X. Zhan, F. Chen, Preparation and performance of amphiphilic polyurethane copolymers with capsaicin-mimic and peg moieties for protein resistance and antibacteria, Industrial & Engineering Chemistry Research, 54 (2015) 3813-3820.
[29] A.Y. Booshehri, R. Wang, R. Xu, Simple method of deposition of CuO nanoparticles on a cellulose paper and its antibacterial activity, Chemical Engineering Journal, 262 (2015) 999-1008.
[30] M. Ben-Sasson, K.R. Zodrow, Q. Genggeng, Y. Kang, E.P. Giannelis, M. Elimelech, Surface functionalization of thin-film composite membranes with copper nanoparticles for antimicrobial surface properties, Environmental science & technology, 48 (2014) 384-393.
[31] M. Sharma, G. Madras, S. Bose, Unique nanoporous antibacterial membranes derived through crystallization induced phase separation in PVDF/PMMA blends, Journal of Materials Chemistry A, 3 (2015) 5991-6003.
[32] D.L. Shaffer, H. Jaramillo, S.R.-V. Castrillón, X. Lu, M. Elimelech, Post-fabrication modification of forward osmosis membranes with a poly (ethylene glycol) block copolymer for improved organic fouling resistance, Journal of membrane science, 490 (2015) 209-219.
[33] J. Wang, Z. Wang, J. Wang, S. Wang, Improving the water flux and bio-fouling resistance of reverse osmosis (RO) membrane through surface modification by zwitterionic polymer, Journal of Membrane Science, 493 (2015) 188-199.
[34] J.L. Watts, Anti-fouling coating composition containing capsaicin, in, Google Patents, 1995.
[35] L. Zhang, J. Xu, Y. Tang, J. Hou, L. Yu, C. Gao, A novel long-lasting antifouling membrane modified with bifunctional capsaicin-mimic moieties via in situ polymerization for efficient water purification, Journal of Materials Chemistry A, 4 (2016) 10352-10362.
[36] S. Kappachery, D. Paul, J. Yoon, J.H. Kweon, Vanillin, a potential agent to prevent biofouling of reverse osmosis membrane, Biofouling, 26 (2010) 667-672.
[37] M. Esmaeili, J. Lahti, T. Virtanen, M. Mänttäri, M. Kallioinen, The interplay role of vanillin, water, and coagulation bath temperature on formation of antifouling polyethersulfone (PES) membranes: Application in wood extract treatment, Separation and Purification Technology, 235 (2020) 116225.
[38] N. Ahmad, A. Samavati, N.A.H.M. Nordin, J. Jaafar, A.F. Ismail, N.A.N.N. Malek, Enhanced performance and antibacterial properties of amine-functionalized ZIF-8-decorated GO for ultrafiltration membrane, Separation and Purification Technology, 239 (2020) 116554.
[39] M. He, X. Fan, Z. Yang, R. Zhang, Y. Liu, L. Fan, Q. Zhang, Y. Su, Z. Jiang, Antifouling high-flux membranes via surface segregation and phase separation controlled by the synergy of hydrophobic and hydrogen bond interactions, Journal of Membrane Science, 520 (2016) 814-822.
[40] S. Déon, A. Escoda, P. Fievet, P. Dutournié, P. Bourseau, How to use a multi-ionic transport model to fully predict rejection of mineral salts by nanofiltration membranes, Chemical Engineering Journal, 189 (2012) 24-31.
[41] P. Dutournié, S. Déon, L. Limousy, Understanding the separation of anion mixtures by TiO2 membranes: Numerical investigation and effect of alkaline treatment on physicochemical properties, Chemical Engineering Journal, 363 (2019) 365-373.
[42] W.R. Bowen, A.W. Mohammad, N. Hilal, Characterization of nanofiltration membranes for predictive purposes—use of salts, uncharged solutes and atomic force microscopy, Journal of membrane science, 126 (1997) 91-105.
[43] S. Déon, A. Escoda, P. Fievet, R. Salut, Prediction of single salt rejection by NF membranes: An experimental methodology to assess physical parameters from membrane and streaming potentials, Desalination, 315 (2013) 37-45.
[44] M.D. Afonso, G. Hagmeyer, R. Gimbel, Streaming potential measurements to assess the variation of nanofiltration membranes surface charge with the concentration of salt solutions, Separation and Purification Technology, 22 (2001) 529-541.

[45] H. Peng, H. Xiong, J. Li, M. Xie, Y. Liu, C. Bai, L. Chen, Vanillin cross-linked chitosan microspheres for controlled release of resveratrol, Food chemistry, 121 (2010) 23-28.
[46] M. Jyothi, S. Yadav, G. Balakrishna, Effective recovery of acids from egg waste incorporated PSf membranes: A step towards sustainable development, Journal of Membrane Science, 549 (2018) 227-235.
[47] S. Mazinani, S. Darvishmanesh, A. Ehsanzadeh, B. Van der Bruggen, Phase separation analysis of Extem/solvent/non-solvent systems and relation with membrane morphology, Journal of Membrane Science, 526 (2017) 301-314.
[48] Z. Xu, J. Liao, H. Tang, J.E. Efome, N. Li, Preparation and antifouling property improvement of Tröger's base polymer ultrafiltration membrane, Journal of Membrane Science, 561 (2018) 59-68.
[49] T.A. Otitoju, A.L. Ahmad, B.S. Ooi, Recent advances in hydrophilic modification and performance of polyethersulfone (PES) membrane via additive blending, RSC advances, 8 (2018) 22710-22728.
[50] M.A. Zazouli, S. Nasseri, M. Ulbricht, Fouling effects of humic and alginic acids in nanofiltration and influence of solution composition, Desalination, 250 (2010) 688-692.
[51] J. Yin, B. Deng, Polymer-matrix nanocomposite membranes for water treatment, Journal of membrane science, 479 (2015) 256-275.
[52] C. Zhao, X. Xu, J. Chen, F. Yang, Effect of graphene oxide concentration on the morphologies and antifouling properties of PVDF ultrafiltration membranes, Journal of Environmental Chemical Engineering, 1 (2013) 349-354.
[53] C. Wu, Y. Wu, J. Luo, T. Xu, Y. Fu, Anion exchange hybrid membranes from PVA and multi-alkoxy silicon copolymer tailored for diffusion dialysis process, Journal of Membrane Science, 356 (2010) 96-104.
[54] D.-X. Wang, M. Su, Z.-Y. Yu, X.-L. Wang, M. Ando, T. Shintani, Separation performance of a nanofiltration membrane influenced by species and concentration of ions, Desalination, 175 (2005) 219-225.
[55] Y.-F. Mi, G. Xu, Y.-S. Guo, B. Wu, Q.-F. An, Development of antifouling nanofiltration membrane with zwitterionic functionalized monomer for efficient dye/salt selective separation, Journal of Membrane Science, 601 (2020) 117795.
[56] S.T. Kelly, A.L. Zydney, Mechanisms for BSA fouling during microfiltration, Journal of Membrane Science, 107 (1995) 115-127.
[57] M.J. Luján-Facundo, J.A. Mendoza-Roca, B. Cuartas-Uribe, S. Álvarez-Blanco, Evaluation of cleaning efficiency of ultrafiltration membranes fouled by BSA using FTIR–ATR as a tool, Journal of Food Engineering, 163 (2015) 1-8.